FULL PAPER

Batteries

ADVANCED
ENERGY
MATERIALS

www.advenergymat.de

Biomimetic Bipolar Microcapsules Derived from *Staphylococcus aureus* for Enhanced Properties of Lithium–Sulfur Battery Cathodes

Wenlu Wu, Jun Pu, Jian Wang, Zihan Shen, Haiyan Tang, Zhentao Deng, Xinyong Tao, Feng Pan, and Huigang Zhang*

Lithium–sulfur (Li–S) batteries suffer from some serious issues, such as volume expansion, polysulfide migration, and so on, which lead to inferior rate properties, low Coulombic efficiency, and poor cycling stability. To a great extent, the significantly changing polarities, conductivities, and solubilities of sulfur species complicate these issues and make them hard to deal with. In this study, a biomimetic bipolar microcapsule is developed via bacteria fermentation and chemical modification. The biomimetic hierarchical microcapsule has a nonpolar core to load active materials and a polar shell to "selectively" control mass transport in and out. Each capsule acts as a microreactor, which adsorbs sulfur with the porous carbon core, retards polysulfide migration with the polar TiO_2 shell, and only facilitates lithium ion diffusion through the shell. The advantages of bipolar microcapsules are able to concurrently address S hosting, electron conducting, and polysulfide migration issues in particle scales instead of electrode scales. Because the resulting sulfur cathodes effectively interact with all sulfur species and confine them inside microcapsules, those intractable issues that lead to poor cycling properties are significantly managed. Thus, a high specific capacity and excellent cycling stability are achieved by using this novel structure design.

1. Introduction

Lithium–sulfur (Li–S) batteries are receiving the increasing attention because of their high energy density, environmental friendliness, low cost, and natural abundance of sulfur

resources. These advantages are highly desired for fast-developing electrical vehicles and large-scale smart grids.[1,2] Although Li–S batteries demonstrate very promising properties, the practical applications of Li–S batteries are still hindered by several scientific and technologic issues, such as the insulating properties of sulfur and discharged products (Li_2S_2/Li_2S), the large volume changes, and the dissolution of polysulfide intermediates (Li_2S_n, $4 \leq n \leq 8$). These issues lead to poor cycling stability, inferior rate capability, and low Coulombic efficiency.[3–5] Improving these electrochemical properties demands a mechanically stable electrode structure, which is able to accommodate the volume change, prevent polysulfides migration, and retain the continuous networks for both electron and ion transports during cycling. However, the charged and discharged products have the opposite polarities, insulating properties, changing volume, and varying solubilities in electrolytes. These changing properties complicate the Li–S design and operation and pose serious challenges to Li–S batteries. Previous studies reported some important approaches to addressing each of those issues separately in the past few years.[6–9]

For example, meso/microporous carbons,[10,11] hollow carbon,[12,13] graphene foam,[14,15] carbon nanotube,[16] and metallic mesh[17] were proposed to host sulfur and polysulfides. These conducting structures are able to provide the rapid electron pathway. Their hollow structures are designed to accommodate the volume change and physically trap polysulfides. The resulting composite sulfur cathodes prolong the cycle lives and increase the specific capacities. However, nonpolar carbon usually repels polysulfides but absorbs sulfur. Recent studies reported that some polar compounds such as metal oxides[18] (TiO_2,[19,20] MnO_2,[21] MgO,[22] and V_2O_5[23,24]) and sulfides (such as CoS_2,[25] Co_3S_4,[26,27] Co_9S_8,[28] and WS_2[29]) demonstrated the strong affinity to polysulfides. Sulfur cathodes with adding these polar compounds could significantly improve the capacity retention of Li–S batteries. As shown in **Figure 1**a, TiO_2 and carbon are used to exemplify how polar and nonpolar materials interact with sulfur and polysulfides, respectively. Melt sulfur wets carbon easily as compared with TiO_2, indicating the

W. Wu, J. Pu, J. Wang, Z. Shen, H. Tang, Prof. Z. Deng, Prof. H. Zhang
National Laboratory of Solid State Microstructures
College of Engineering and Applied Sciences
Collaborative Innovation Center of Advanced Microstructures
and Institute of Materials Engineering
Nanjing University
Jiangsu 210093, China
E-mail: hgzhang@nju.edu.cn
Prof. X. Tao
College of Materials Science and Engineering
Zhejiang University of Technology
Hangzhou 310014, China
Prof. F. Pan
School of Advanced Materials
Peking University
Shenzhen Graduate School
Shenzhen 518055, China

1702373 (1 of 9)

**ADVANCED
SCIENCE NEWS**
www.advancedsciencenews.com

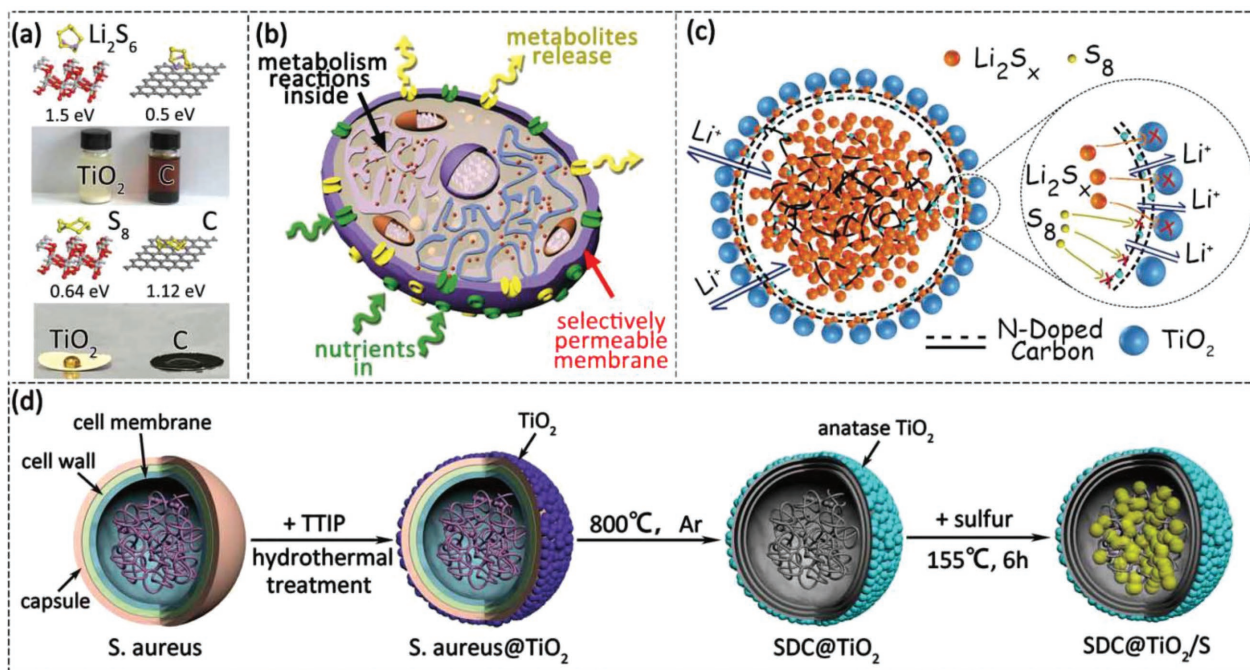**ADVANCED
ENERGY
MATERIALS**
www.advenergymat.de

Figure 1. a) Binding energy calculation and interaction experiments between adsorbents (TiO_2 and carbon) and sulfur species (S_8 and Li_2S_6). b) A cell example, which illustrates reactions and substances transport, in a biologic system. c) Biomimetic microcapsules, which are able to facilitate Li-ion transport and confine both sulfur and polysulfide through the strong interactions as exemplified in (a). d) Schematic illustration of the synthetic procedure for the biomimetic microcapsule confined sulfur cathodes.

strong interaction. The quick adsorption of Li_2S_6 in Figure 1a indicates that polar TiO_2 adsorbs polysulfides more effectively than nonpolar carbon. The first-principle calculation confirms that sulfur or polysulfides interact strongly with the adsorbents, which have the similar polarity as them, respectively. Because the sulfur-related species (S_8, Li_2S_x, $x = 1$–8) inside cathodes have such varied polarities, conductivity, and solubility, it is difficult to address the dissolution and migration issues by confining or localizing the sulfur species with only one type of interaction. Polar polymer-modified carbon[30,31] and amphiphilic molecules[32] have been proposed to improve the cycling performance by enhancing the polysulfide adsorption.

Although the amphiphilic concept or simply mixing adsorbents with different polarities is able to improve the Li–S battery performance, how to efficiently integrate the polar and nonpolar interactions in one electrode remains a challenge for Li–S batteries. Either polymer molecules or metal oxides/sulfides show very limited surface adsorption sites as compared with the vast numbers of loaded sulfur species. It is not suggested to add many absorbents. Excess absorbents relatively decrease the specific capacity due to the increased inactive mass. In addition, polysulfide migration is hard to control along the edges or sides of the conventional cells by applying adsorbents onto separators or directly mixing them into cathodes.

In contrast, biologic systems provide excellent examples to direct mass transport and localize biologic reactions with high efficiencies of nutrients conversion and metabolites release. As shown in Figure 1b, a biologic cell has central microreaction "factories," which are separated by selectively permeable membranes from outside environment. The external membrane

controls the mass transport of substances in and out of cells. Only necessary nutrients are allowed into cells and metabolites released to the environment through the membrane protein interaction with substances. The selective transport and confined reaction are desired for the ideal Li–S reaction.

In this work, we are inspired by cell structures and propose a biomimetic microcapsule as shown in Figure 1c. Polar TiO_2 is used as the model chemical to build the biomimetic membrane, which allows lithium ion diffusion and mitigates polysulfides migration by means of the strong adsorption. The carbonaceous interior is derived from *Staphylococcus aureus* (*S. aureus*) via a microbial fermentation and heat treatment route. The porous carbon is designed to host and adsorb sulfur. The sulfur cathodes with bipolar microcapsule confinement demonstrate a high capacity of 1202 mA h g^{-1} and the good cycling properties.

2. Results and Discussion

Figure 1d illustrates the fabrication procedure of biomimetic microcapsule-confined sulfur cathodes. First, *S. aureus* was cultured in lysogeny broth (LB) as shown in the Figure S1a in the Supporting Information. After about 18 h fermentation, the flask (Figure S1b, Supporting Information) was colonized with golden-yellow *S. aureus*, which is a round-shaped bacterium (**Figure 2**a). Figure S2 in the Supporting Information illustrates that *S. aureus* generally comprises of a secreted capsule, cell wall, cell membrane, cytoplasm, circular chromosome, etc.[33] These structural elements are assembled in a hierarchical microcapsule. On the surface of *S. aureus,* there are some
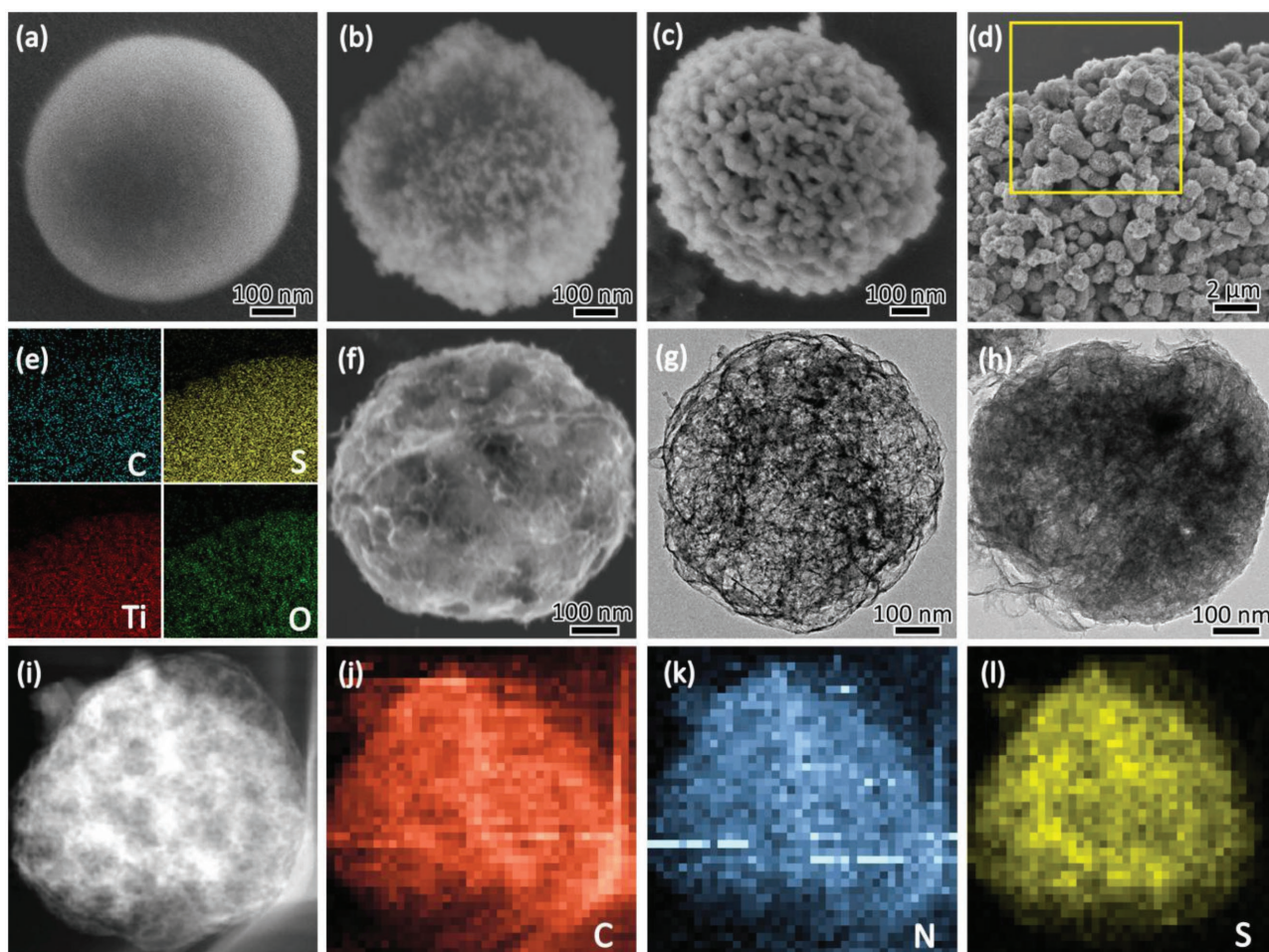
ADVANCED
SCIENCE NEWS
www.advancedsciencenews.com

ADVANCED
ENERGY
MATERIALS
www.advenergymat.de

Figure 2. SEM images of a) *S. aureus*, b) *S. aureus*@TiO_2, c) SDC@TiO_2, and d) SDC@TiO_2/S. e) Elemental mapping of SDC@TiO_2/S. f) SEM and g) TEM images of SDC. h) TEM and i) STEM images of SDC/S. j–l) Elemental mapping of SDC/S.

secreted polysaccharides and proteins, which act as the binding ligands to colonize host tissue. We dispersed the cultured *S. aureus* in *n*-butyl alcohol and utilized the surface binding anchors to nucleate TiO_2 precursor, which was produced by hydrolyzing titanium tetraisopropoxide (TTIP) in an autoclave. After filtration, the isolated particles were annealed at 800 °C to crystallize anatase TiO_2 on the surface of carbonized *S. aureus*. Because the bacteria had abundant carbon and nitrogen, carbonization resulted in the formation of N-doped carbon, which was also desired to anchor polysulfides.[34–36] Bacteria cytoplasm consisted of water and organic structural elements as shown in Figure S2 in the Supporting Information. During carbonization, water evaporated and led to the porous interiors. This carbonized structure was called *S. aureus*-derived carbon (SDC). In the last step, TiO_2-coated SDC was impregnated with sulfur through a conventional melt-diffusion approach to form a composite particle of SDC@TiO_2/S.[37]

Figure 2a shows that the diameter of a single *S. aureus* is ≈600 nm. Figure S3 in the Supporting Information presents the scanning electron microscopy (SEM) images of monodispersed and clustered *S. aureus*. When the cell autolysin is inhibited or absent during the proliferation, the daughter cell remains

closely attached to one another.[38] Thus, *S. aureus* aggregates usually appear as grape-like clusters, which can be seen from Figure S3b in the Supporting Information. The connected clusters are favorable from the perspective of the battery electrode fabrication because carbonizing the connected clusters lead to a continuous electron pathway, and the large clusters enable a high tap density. Figure 2b presents the typical morphology of TiO_2 nanoparticle-coated *S. aureus,* which was isolated from the autoclave after the hydrothermal reaction. The following heat treatment converted *S. aureus* to SDC. About 20 nm TiO_2 was crystallized on the external surface of SDC (Figure 2c). These TiO_2 nanocrystals aggregate to form a hard shell, which may act as the mechanical support and maintain the stable particulate structures. The external TiO_2 shell is polar and internal carbon is nonpolar, yielding a bipolar microcapsule. Such a hierarchical microsphere is labeled as SDC@TiO_2. Sulfur was then infilled into the hierarchical pores of SDC@TiO_2 via a conventional melt-diffusion approach. This bipolar structure promotes the sulfur absorption into SDC because polar TiO_2 repels but carbon attracts sulfur. Figure 2d shows that sulfur-loaded SDC@TiO_2 generally retains the spherical morphology. The corresponding energy dispersive X-ray spectroscopic (EDX)

**ADVANCED
SCIENCE NEWS**
www.advancedsciencenews.com

**ADVANCED
ENERGY
MATERIALS**
www.advenergymat.de

mapping indicates the uniform distribution of carbon, titanium, oxygen, and sulfur in the aggregates of SDC@TiO$_2$/S particles (Figure 2e). Figure S4a–c shows the corresponding optical photographs.

It should be noted that the direct heat treatment of *S. aureus* powders would result in the morphological collapse of spherical *S. aureus* (Figure S5, Supporting Information). The collapse might relate to the chemical composition of *S. aureus*. The structural collapse will lead to the failure of the concept of biomimetic microcapsule design. TiO$_2$ as the protection layer is able to prevent the structural collapse. We will address the importance of the microcapsule structure in the following section.

To further observe the SDC morphology and to investigate the spatial distribution of sulfur inside a particle, the TiO$_2$ shell was selectively removed by dilute hydrofluoric acid (HF). Figure 2f shows that the spherical shape is basically retained. The transmission electron microscopic (TEM) image in Figure 2g indicates that the heat treatment converted the structural elements such as cell wall, membrane, nucleoid, etc. into a porous network. Figure 2h shows the TEM image of sulfur-loaded SDC. Under the scanning TEM (STEM) mode, the bright regions in Figure 2i indicate heavy elements. Figure 2j,k shows that SDC comprises of carbon and abundant nitrogen, indicating that the heat-treated *S. aureus* turns to be N-doped carbon. Because bacteria consist of abundant N-containing organic chemicals such as protein, nucleic acid, peptidoglycan, it is easy to yield N-doped carbon by heat treatment. The element mapping in Figure 2l clearly confirms that sulfur is uniformly distributed inside SDC, indicating that the porous structure is able to effectively absorb and confine elemental sulfur.

Figure 3a shows that the X-ray diffraction (XRD) pattern of SDC is in agreement with amorphous carbon. All the identified peaks of SDC@TiO$_2$ can be assigned to the anatase TiO$_2$ phase (JCPDS Card no. 21–1272). As shown in Figure 3b, the Raman spectra of SDC@TiO$_2$ and SDC@TiO$_2$/S exhibit the typical peaks at ≈1345 and 1590 cm^{-1}, which are due to the D and G bands of carbon materials, respectively.[39,40] The sharp peak at 148 cm^{-1} and three small peaks nearby 500 cm^{-1} are due to typical anatase TiO$_2$.[41] The bending and stretching modes of pure sulfur appear below 500 cm^{-1}.[42] The peaks at ≈200 and 500 cm^{-1} are barely observable because a great proportion of S with dimensions on the nanoscale is buried in the carbonaceous matrix.[43] The sulfur content in SDC@TiO$_2$/S is estimated to be 74 wt% according to the thermogravimetric analysis (TGA) in Figure S6 in the Supporting Information. Figure 3c,d shows the nitrogen adsorption and desorption isotherms of SDC and SDC@TiO$_2$. The Barrett–Emmett–Teller surface areas of SDC and SDC@TiO$_2$ are 651.2 and 131.4 m^2 g^{-1}, respectively. The decrease of surface area is due to the heavy mass of TiO$_2$ nanoparticles. The Barrett–Joyner–Halenda analysis determines the pore size distribution of SDC to be 3–17 nm. The pore size distribution of SDC@TiO$_2$ basically retains the pore structure of SDC as shown in Figure 3d.

The X-ray photoelectron spectroscopy (XPS) measurements were conducted to investigate the chemical composition of SDC and SDC@TiO$_2$. The survey spectrum in Figure 3e distinctly reveals that SDC consists of a large amount of carbon element and small ratios of nitrogen and oxygen. The N 1s spectrum can be fitted into three peaks at 397.9, 400.4, and 401.5 eV, which correspond to the pyridinic, pyrrolic, and quaternary N, respectively.[44–46] The quantitative element analysis concludes
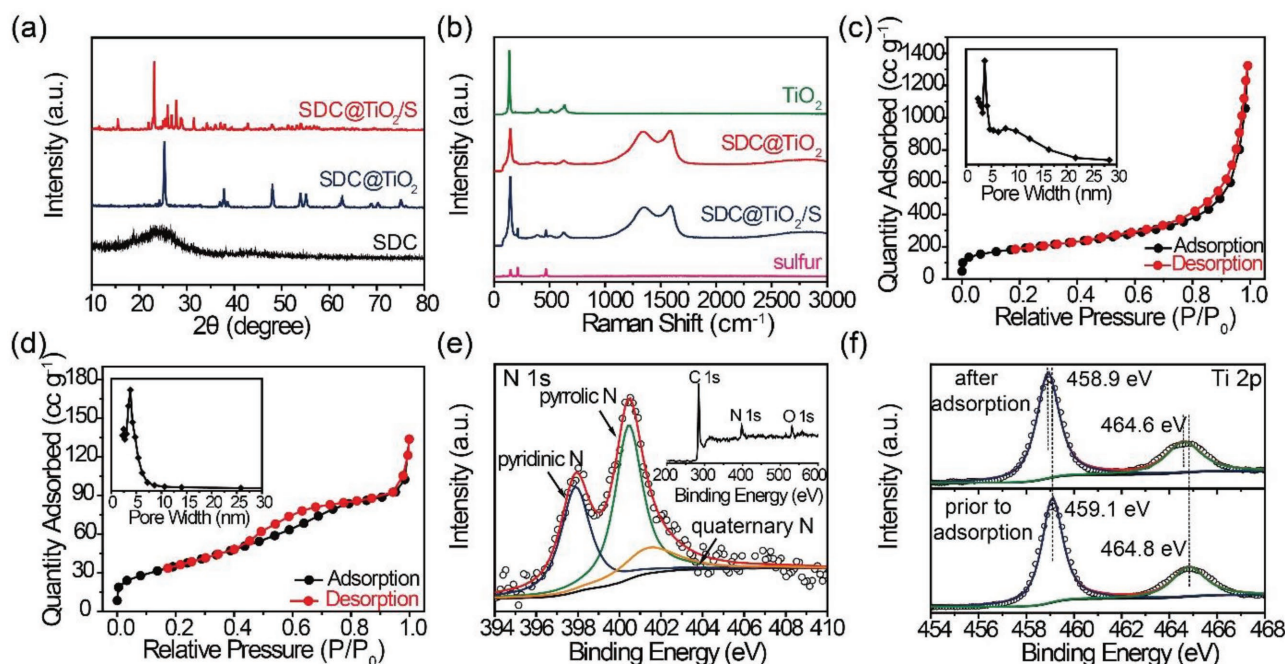

Figure 3. a) XRD patterns of SDC, SDC@TiO$_2$, and SDC@TiO$_2$/S. b) Raman spectra of TiO$_2$, SDC@TiO$_2$, SDC@TiO$_2$/S, and sulfur. Nitrogen adsorption isotherms and pore–size distributions of c) SDC and d) SDC@TiO$_2$. XPS spectra of e) N 1s signal of SDC (inset: the survey spectrum of SDC), f) Ti 2p signals of SDC@TiO$_2$ prior to and after Li$_2$S$_6$ adsorption tests.

ADVANCED
SCIENCE NEWS

www.advancedsciencenews.com

ADVANCED
ENERGY
MATERIALS

www.advenergymat.de

that the nitrogen percentage is about 3.4 at%. According to previous reports,[47,48] pyridinic and pyrrolic nitrogens are favorable to immobilize polysulfide intermediates. Figure 3f shows the Ti 2p spectra of SDC@TiO$_2$ prior to and after the adsorption tests in the electrolyte containing Li$_2$S$_6$. The two characteristic peaks at 459.1 and 464.8 eV are ascribed to Ti 2p$_{3/2}$ and Ti 2p$_{1/2}$ signals by spin–orbit splitting, suggesting the existence of fully oxidized Ti^{4+} in TiO$_2$.[49] It can be observed that there is a small shift of −0.2 eV to lower binding energy in the Ti 2p spectrum of SDC@TiO$_2$ after Li$_2$S$_6$ adsorption test. It indicates the strong interaction between Li$_2$S$_6$ and TiO$_2$ because of the electron donation from sulfides to Ti^{4+}.[50,51] This interaction is able to mitigate the polysulfide migration. The TiO$_2$ shell could block the polysulfide diffusion through the strong adsorption.

To verify whether the TiO$_2$ shell could act as a selectively permeable layer just as a cytomembrane does, the permeability tests were conducted within an H-cell (Figure S7b,e, Supporting Information) whose two chambers were separated by a TiO$_2$-coated filter paper. The same solvents as used in Li–S battery electrolyte were first added to the two chambers. After adding the bis-(trifluoromethane) sulfonimide lithium (LiTFSI) in the left chamber, the cyclic voltammetric (CV) scanning between two Pt wires within the left chamber shows a rectangle shape (Figure S7a, Supporting Information), which results from the electrochemical double layer charging. As compared with the almost zero current for pure solvents, the increased current response indicates that the solution was conductive because of the LiTFSI addition. Figure S7c in the Supporting Information shows that after 20 min, the initially nonconductive solution in the right chamber also turned to be conductive, indicating that LiTFSI diffuses through the TiO$_2$ separator. In the control experiment (Figure S7d–f, Supporting Information), LiTFSI was replaced with polysulfides (Li$_2$S$_x$). The sloping CV curves in the left chamber after adding polysulfides indicate the electrocatalytic reactions, which differ from the nonfaradaic charging mechanism. After 20 min, the solution in the right chamber still shows the almost zero current response, indicating that polysulfides were blocked in the left chamber by the TiO$_2$ separator. In general, Figure S7 in the Supporting Information confirms that the TiO$_2$ layer is able to act as a selectively permeable membrane and indirectly verifies the design concept.

To determine if the biomimetic structure could effectively improve the battery performance, SDC@TiO$_2$/S and several control samples were assembled with lithium into coin cells, respectively. SDC was simply mixed with sulfur via the conventional melt-diffusion route to form an SDC/S sample, which has only nonpolar carbon with N-doping for sulfur species adsorption. TiO$_2$ nanoparticles as polar adsorbents were mixed with sulfur to produce the TiO$_2$/S sample. A pure S sample was fabricated by mixing acetylene black (AB) and sulfur. The sulfur load is controlled around 2.5 mg cm^{-2} for all four samples. To eliminate the capacity contribution from TiO$_2$ lithiation, the discharge voltage cutoff was set at 1.8 V (Figure S8, Supporting Information).[52] **Figure 4**a shows the galvanostatic charge–discharge curves of the four samples at the current density of 0.1 A g^{-1}. Two reaction plateaus can be clearly observed in the discharge curves of all the four cathodes and agree well with the typical multistep reduction of sulfur. The first voltage plateau at ≈2.35 V is considered as the conversion from S$_8$ to the soluble polysulfides Li$_2$S$_n$ (4 ≤ n ≤ 8).

The lower plateau at ≈2.1 V is due to the reactions from Li$_2$S$_n$ (4 ≤ n ≤ 8) into the insoluble products Li$_2$S$_2$ or Li$_2$S.[53,54] The high discharge plateaus of TiO$_2$/S and SDC@TiO$_2$/S imply that the adsorption effect of polar TiO$_2$ lowers the polysulfides concentration in electrolytes and increases the discharge voltages.[55] In the charging process, the first long and flat plateau presents the oxidation of insoluble Li$_2$S$_2$/Li$_2$S to soluble polysulfide species. At 0.1 A g^{-1}, SDC@TiO$_2$/S, SDC/S, TiO$_2$/S, and pure S cathodes deliver the discharge capacities of 1202, 1133, 975, and 918 mA h g^{-1}, respectively.

Figure 4b shows the rate properties of the four sulfur cathodes at varied current densities. The SDC@TiO$_2$/S cathode has the high capacity retention at high rates, indicating the best rate capability. At 1.5 A g^{-1}, it delivers a capacity of 845 mA h g^{-1}, which corresponds to 70.3% of its low rate capacity at 0.1 A g^{-1}. In contrast, the capacity retentions of SDC/S, TiO$_2$/S, and pure S are only 57.3%, 35.5%, and 4.3%, respectively. When the current density returns to 0.1 A g^{-1}, the SDC@TiO$_2$/S cathode can still deliver a reversible capacity of 1110 mA h g^{-1}, which accounts for 92.3% of its initial capacity. For the SDC/S cathode, the lowered current density could only recover a reversible capacity of 868 mA h g^{-1}, which is equal to about 77.3% of its initial capacity at the same rate.

By comparing the curves of the samples with and without TiO$_2$, it could be found that the samples containing TiO$_2$ components have the relatively high rate performance. The reasons were already revealed in previous studies.[19,43] First, TiO$_2$ nanoparticles can adsorb polysulfides and limit their migration.[51,56] Second, TiO$_2$ can also catalyze the conversion of polysulfides.[55,57] The good rate capability of SDC samples could be attributed to the microcapsule structure, which spatially localizes polysulfides inside and maintains the integrity and stability of the electrodes during the lithiation/delithiation process. It is worth noting that the rate performance of SDC/S is better than the TiO$_2$/S cathode. The reasons may be deduced from two aspects. First, TiO$_2$ has intrinsically low electron conductivity (10^{-12}–10^{-7} cm^2 S^{-1}),[58,59] which could reduce the cycling kinetics if they are not effectively wired. Second, the total adsorption sites of TiO$_2$ nanoparticles are generally not high enough to suppress all the polysulfides migration if they are not appropriately arranged in 3D structures. These two reasons may lead to the increased polarization and the capacity loss. The microcapsule structure of SDC@TiO$_2$/S could maximize the confinement effects by using a low fraction of TiO$_2$ on the shell. The external TiO$_2$ shell acts as a "sieve" to allow the Li$^+$ diffusion and however, retard polysulfide migration.

Figure 4c shows the cycling properties of the four samples at 0.2 A g^{-1}. After 100 cycles, the SDC@TiO$_2$/S, SDC/S, TiO$_2$/S, and pure S cathodes deliver the capacities of 1040, 793, 691, and 261 mA h g^{-1}, respectively. Figure 4d shows that SDC@TiO$_2$/S, SDC/S, TiO$_2$/S, and pure S cathodes lose the capacities of 140, 335, 265, and 572 mA h g^{-1} during 100 cycles, respectively. By contrast, the sulfur utilization for the SDC@TiO$_2$/S cathode reaches ≈70.6%, which is greater than other three electrodes. Apparently, the biomimetic microcapsule-confined sulfur cathode demonstrates the highest capacity and lowest loss during cycling.

To confirm the role of microcapsule structure, we intentionally destroyed the hierarchical structures by excessively
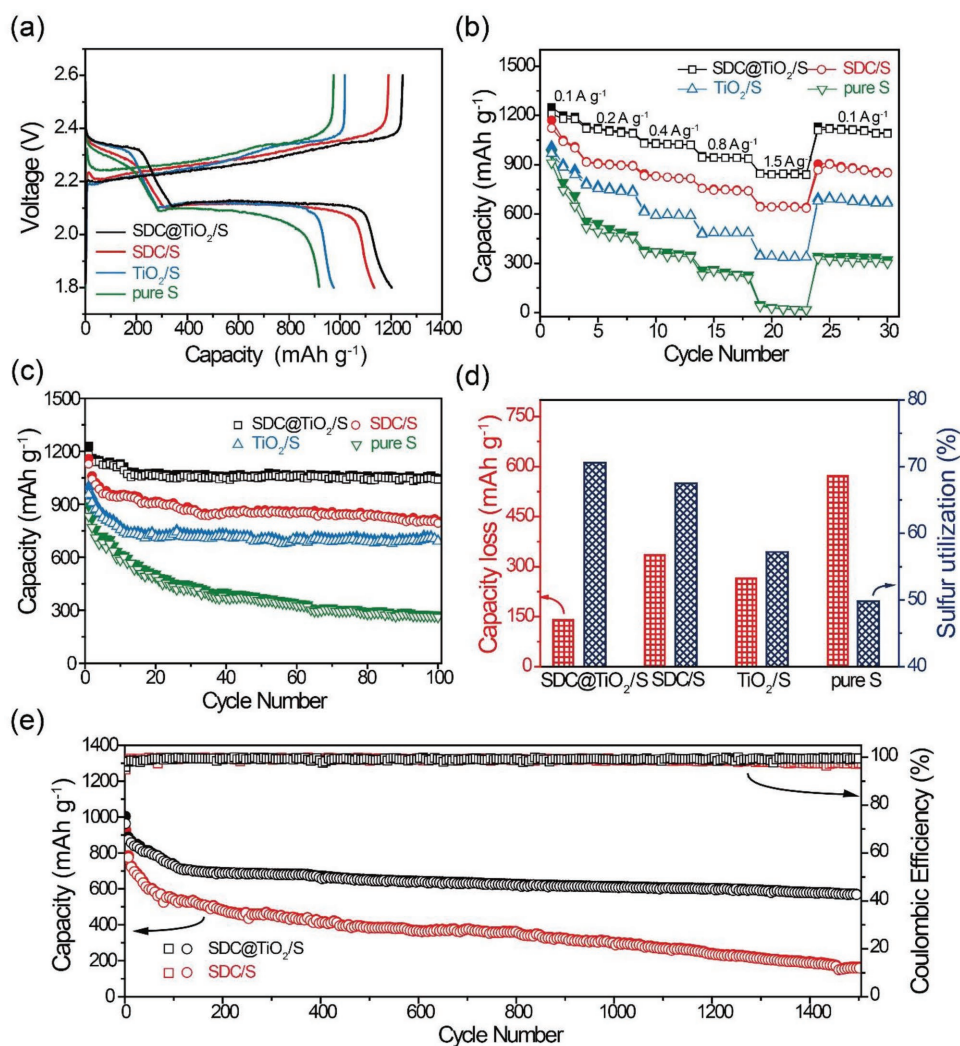
**ADVANCED
SCIENCE NEWS**

www.advancedsciencenews.com

**ADVANCED
ENERGY
MATERIALS**

www.advenergymat.de

Figure 4. a) Discharge/charge curves of the SDC@TiO$_2$/S, SDC/S, TiO$_2$/S, and pure S cathodes at 0.1 A g^{-1}, b) rate capabilities of the four cathodes at varied current densities, c) cycling properties of the four cathodes at 0.2 A g^{-1} for 100 cycles, d) capacity loss after 100 cycles and sulfur utilization of the four cathodes, e) long-term cycling properties of SDC@TiO$_2$/S and SDC/S cathodes at 1.5 A g^{-1} over 1500 cycles.

milling. Figure S9a in the Supporting Information shows the SEM image of broken SDC@TiO$_2$/S. The EDX element mapping in Figure S9b–e in the Supporting Information further confirms the hierarchical structure of bipolar microcapsule-confined sulfur cathodes. Because the broken microcapsules let sulfur cores expose and lose the selectively permeable effect of the TiO$_2$ shell, the cycling properties in Figure S9f in the Supporting Information degrade significantly as compared with its counterpart sample in Figure 4c. It is understandable that the broken microcapsules differ little from the sample, which was prepared by simply mixing TiO$_2$ nanoparticles with broken SDC/S. Therefore, the 3D bipolar microcapsule design is of vital importance because it spatially suppresses polysulfide migration and enhances the electrochemical properties of Li–S batteries.

A long-term cycling was tested at a high rate of 1.5 A g^{-1} for SDC@TiO$_2$/S and SDC/S cathodes. Figure 4e shows that both SDC@TiO$_2$/S and SDC/S exhibit a relatively rapid capacity decay in the first 100 cycles. SDC/S loses 15% more capacity

than SDC@TiO$_2$/S in this stage. After the rapid decay in the first few cycles, SDC@TiO$_2$/S and SDC/S gradually approach the relatively stable cycling stage, in which the average capacity loss rates are around 0.016% and 0.050% per cycle, respectively. After 1500 cycles, SDC@TiO$_2$/S is still able to deliver 569 mA h g^{-1}, which is much higher than that of SDC/S (159 mA h g^{-1}). It should be noted that high rate cycling might cause the degradation of lithium metal anodes, although the counter electrode is usually highly overmatched. The capacity loss may result from the anode side. The Coulombic efficiency of SDC@TiO$_2$/S increases from 96% in the 1st cycle to 99% in the 20th cycle and maintains almost 99.5% until 1500 cycles. SDC/S also demonstrates the increased Coulombic efficiency initially. However, the Coulombic efficiency of SDC/S is not stable. It even decreases to ≈97% at last. The relatively poor cycling performance may be related to the slightly incapable control on adsorption and migration issues.

To test the assumption, the polysulfide adsorption capabilities of SDC@TiO$_2$ and SDC were further examined within the

ADVANCED
SCIENCE NEWS
www.advancedsciencenews.com

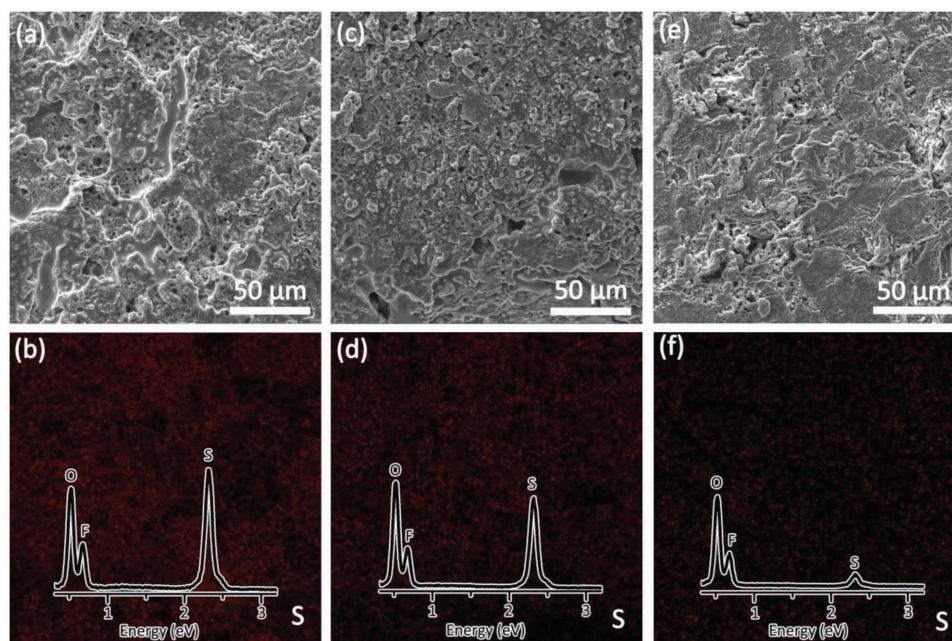**ADVANCED**
ENERGY
MATERIALS
www.advenergymat.de

Figure 5. SEM a,c,e) and EDX mapping b,d,f) images of the anode surfaces of cells, which were cycled with a,b) pure S cathode; c,d) SDC/S cathode; and e,f) SDC@TiO₂/S cathode, respectively.

Li_2S_6-containing electrolyte. Figure S10 in the Supporting Information shows that SDC@TiO₂ exhibits the highest adsorption response to Li_2S_6. As compared with the control sample (AB), SDC only demonstrates a certain degree of adsorption to Li_2S_6, which results from N-doping. This test also indicates that only N-doping in SDC is not enough to adsorb and mitigate polysulfide migration issues. To further verify the deduction, postmortem experiments were conducted on three cells using SDC@TiO₂/S, SDC/S, and pure S cathodes. These three cells were assembled and cycled under the exact same conditions. After 200 cycles, they were disassembled and their anodes were characterized by SEM and EDX technologies. **Figure 5** shows that sulfur distribution is significantly different on the three anodes. It is clearly found that sulfur elements were heavily accumulated on the anode surface of the pure S and SDC/S cells as compared with that of the SDC@TiO₂/S cell. The barely observable sulfur distribution on the anode surface of the SDC@TiO₂/S cell confirms that SDC@TiO₂ is able to effectively confine polysulfides and retard their migration. Therefore, the biomimetic bipolar microcapsule structure is able to effectively mitigate the polysulfide issues. We further increased the sulfur loading to ≈5 mg cm⁻². Figure S11 in the Supporting Information shows the cycling properties. Because of the high loading, the cell was cycled at a relatively low current density (0.2 A g⁻¹). In the first few cycles, the specific capacity increases from 893 to 986 mA h g⁻¹, indicating the gradual accessibility of active materials. Afterward, the specific capacity of SDC@TiO₂/S slowly decreases. Until the 100th cycle, it still delivers a capacity of 791 mA h g⁻¹. We summarized the recent reports about high S loading in Table S1 in the Supporting Information. The capacity retention in Figure S11 in the Supporting Information is modestly high among the previous reports. The self-discharge behavior was studied by monitoring

open circuit voltage of a Li–S cell with an SDC@TiO₂/S cathode (Figure S12, Supporting Information). In two weeks, the cell shows a stable voltage profile, which indicates a low self-discharge rate because of polysulfide migration suppression.

3. Conclusions

In summary, we proposed a biomimetic bipolar microcapsule as the sulfur cathode host and developed a facile fabrication route consisting of microbial fermentation and chemical modification. The hierarchical biomimetic structure is able to effectively and concurrently deal with the varied polarities and dissolution of various sulfur species during charge–discharge processes. Its internal porous carbon is to adsorb and host nonpolar sulfur. Its TiO₂ shell can confine polar polysulfides and retard their migration. Due to these design advantages, the sulfur utilization is significantly improved, and the polysulfide migration is greatly retarded. The SDC@TiO₂/S cathode could deliver a specific capacity of 1202 mA h g⁻¹ at 0.1 A g⁻¹. The long-term cycling demonstrates a low capacity decay rate of 0.016% per cycle at 1.5 A g⁻¹ over 1500 cycles. Last but not the least, TiO₂ is used as a model adsorbent in this study. If some stronger adsorbents or higher efficiency electrocatalysts (for example, V₂O₅,[23,60] VS₂, and TiS₂[61]) are introduced into the microcapsule, the biomimetic capsule-like concept will perform even better as particulate microreactors. The fermentation industries of medicines and some fine chemicals (protein A, erythromycin, amino acids, vitamin, etc.) produce many microorganism wastes (including *S. aureus*). The current biomimetic route could utilize these microorganism dead bodies for sulfur batteries cathodes and make wastes profitable. Thus, the biomimetic approach combining the biologic fermentation

and chemical syntheses will open a new avenue to advance the preparation of high-performance battery electrode materials.

4. Experimental Section

Cultivation of S. aureus: *S. aureus* (ATCC 6538) strains were provided by Cedarlane Laboratories (Burlington, Canada). *S. aureus* was cultured in LB (Sangon Biotech) at 37 °C for 18 h. They were harvested by centrifuging at 4000 rpm for 5 min, washed three times with deionized water.

Synthesis of SDC@TiO$_2$: About 0.2 g *S. aureus* was dispersed into 200 mL *n*-butanol (99.8%, Sigma-Aldrich), and 4 g hexadecylamine (HDA, 90%, Aladdin) was dissolved into the suspension. About 4.5 mL TTIP (97%, Aladdin) and 1.6 mL aqueous NH$_4$Cl solution (0.1 M) were added to the mixture, which was stirred at 25 °C for 2 min and kept static at room temperature for 18 h. The solid particles were collected by centrifugation and washed with ethanol (>99.5%, Sigma-Aldrich). The obtained powder was redispersed in a mixture of 20 mL ethanol, 10 mL deionized water, and 1 mL ammonia (28 wt%, Sigma-Aldrich). The resulting mixture was sealed within a 50 mL Teflon-lined autoclave and heated at 160 °C for 16 h. After hydrothermal reaction, the solid products were centrifuged, washed, and dried. To prepare SDC@TiO$_2$, the dried powder was carbonized under Ar atmosphere at 800 °C for 2 h. Anatase TiO$_2$ nanoparticles were prepared using the same approach without adding *S. aureus*.

Synthesis of SDC@TiO$_2$/S, SDC/S, and TiO$_2$/S Composites: The SDC@TiO$_2$/S, SDC/S, and TiO$_2$/S composites were prepared via a conventional melt-diffusion approach.[37] Sulfur was mixed with SDC@TiO$_2$, SDC, and TiO$_2$ nanoparticles. The obtained mixtures were heated at 155 °C in a sealed container for 6 h under Ar atmosphere to let sulfur diffuse.

Material Characterization: XRD patterns of all samples were collected by a Rigaku D/Max III with Cu Kα radiation. The morphology observation was conducted within a Zeiss Ultra 55 field-emission SEM. XPS spectra were recorded on an ESCALab MKII X-ray photoelectron spectrometer with Mg Kα X-ray as the excitation source. TEM and STEM images and EDX spectra were recorded on an FEI Tecnai F20 microscope at 200 kV. The amount of sulfur in the cathode was determined by TGA (NETZSCH 209 F1 Libra thermal analyzer) from room temperature to 500 °C in a nitrogen flow at a heating rate of 10 °C min^{-1}. N$_2$ adsorption measurements were performed on a Quantachrome Autosorb-IQ-2C-TCD-VP analyzer at 77 K.

For the visualized adsorption characterization, a Li$_2$S$_6$ solution was synthesized by adding Li$_2$S and sulfur with a molar ratio of 1:5 in dimethyl ether (DME, Aladdin) under stirring according to literature.[25] The obtained solution containing about 2 mg mL^{-1} Li$_2$S$_6$ was used for the sulfide adsorption test. SDC@TiO$_2$, SDC, and AB were added into 5 mL of Li$_2$S$_6$/DME solutions for comparison, respectively.

Electrochemical Measurement: Sulfur cathodes were fabricated by slurry casting an 8:1:1 mass ratio mixture of active materials, AB, and polyvinylidene fluoride (PVDF) on Al foil. The sulfur loading is controlled around 2–5 mg cm^{-2}. The obtained laminate was dried in vacuum at 50 °C. The SDC@TiO$_2$/S, SDC/S, TiO$_2$/S, and pure S cathodes were assembled with lithium into coin cells in an Ar-filled glove box. The electrolyte used was 1.0 M LiTFSI and 0.1 M LiNO$_3$ with a 1:1 volume ratio of 1,3-dioxolane (DOL) and DME. The volume of the electrolyte was ≈50 μL. Galvanostatic charge–discharge was carried out from 1.8 to 2.6 V using a Land Battery Tester and Bio-Logic potentiostat.

Supporting Information

Supporting Information is available from the Wiley Online Library or from the author.

Conflict of Interest

The authors declare no conflict of interest.

Keywords

[1] T. D. Bogart, D. Oka, X. T. Lu, M. Gu, C. M. Wang, B. A. Korgel, *ACS Nano* **2014**, *8*, 915.

[2] B. Scrosati, J. Garche, *J. Power Sources* **2010**, *195*, 2419.

[3] Y. V. Mikhaylik, J. R. Akridge, *J. Electrochem. Soc.* **2004**, *151*, A1969.

[4] A. Manthiram, Y. Z. Fu, Y. S. Su, *Acc. Chem. Res.* **2013**, *46*, 1125.

[5] P. P. R. M. L. Harks, C. B. Robledo, T. W. Verhallen, P. H. L. Notten, F. M. Mulder, *Adv. Energy Mater.* **2017**, *7*, 1601635.

[6] W. Y. Li, G. Y. Zheng, Y. Yang, Z. W. Seh, N. Liu, Y. Cui, *Proc. Natl. Acad. Sci.* **2013**, *110*, 7148.

[7] S. Y. Wei, L. Ma, K. E. Hendrickson, Z. Y. Tu, L. A. Archer, *J. Am. Chem. Soc.* **2015**, *137*, 12143.

[8] J. T. Zhang, H. Hu, Z. Li, X. W. Lou, *Angew. Chem., Int. Ed.* **2016**, *55*, 3982.

[9] W. Liu, J. B. Jiang, K. R. Yang, Y. Y. Mi, P. Kumaravadivel, Y. R. Zhong, Q. Fan, Z. Weng, Z. S. Wu, J. J. Cha, H. H. Zhou, V. S. Batista, G. W. Brudvig, H. L. Wang, *Proc. Natl. Acad. Sci.* **2017**, *114*, 3578.

[10] Y. Z. Liu, G. R. Li, J. Fu, Z. W. Chen, X. S. Peng, *Angew. Chem., Int. Ed.* **2017**, *56*, 1.

[11] L. Hu, Y. Lu, X. N. Li, J. W. Liang, T. Huang, Y. C. Zhu, Y. T. Qian, *Small* **2017**, *13*, 1603533.

[12] W. D. Zhou, C. M. Wang, Q. L. Zhang, H. D. Abruna, Y. He, J. W. Wang, S. X. Mao, X. C. Xiao, *Adv. Energy Mater.* **2015**, *5*, 1401752.

[13] W. Y. Li, Z. Liang, Z. D. Lu, H. B. Yao, Z. W. Seh, K. Yan, G. Y. Zheng, Y. Cui, *Adv. Energy Mater.* **2015**, *5*, 1500211.

[14] L. W. Ji, M. M. Rao, H. M. Zheng, L. Zhang, Y. C. Li, W. H. Duan, J. H. Guo, E. J. Cairns, Y. G. Zhang, *J. Am. Chem. Soc.* **2011**, *133*, 18522.

[15] G. Y. Xu, Q. B. Yan, A. Kushima, X. G. Zhang, J. Pan, J. Li, *Nano Energy* **2017**, *31*, 568.

[16] J. S. Lee, J. Jun, J. Jang, A. Manthiram, *Small* **2017**, *13*, 1602984.

[17] Y. Y. Mao, G. R. Li, Y. Guo, Z. P. Li, C. D. Liang, X. S. Peng, Z. Lin, *Nat. Commun.* **2017**, *8*, 14628.

[18] X. Liu, J. Q. Huang, Q. Zhang, L. Q. Mai, *Adv. Mater.* **2017**, *7*, 1601759.

[19] Z. W. Seh, W. Y. Li, J. J. Cha, G. Y. Zheng, Y. Yang, M. T. McDowell, P. C. Hsu, Y. Cui, *Nat. Commun.* **2013**, *4*, 1331.

[20] X. W. Wang, T. Gao, X. L. Fan, F. D. Han, Y. Q. Wu, Z. A. Zhang, J. Li, C. S. Wang, *Adv. Funct. Mater.* **2016**, *26*, 7164.

[21] X. Liang, C. Hart, Q. Pang, A. Garsuch, T. Weiss, L. F. Nazar, *Nat. Commun.* **2015**, *6*, 5682.

[22] X. Y. Tao, J. G. Wang, C. Liu, H. T. Wang, H. B. Yao, G. Y. Zheng, Z. W. Seh, Q. X. Cai, W. Y. Li, G. M. Zhou, C. X. Zu, Y. Cui, *Nat. Commun.* **2016**, *7*, 11203.

[23] M. Liu, Q. Li, X. Y. Qin, G. M. Liang, W. J. Han, D. Zhou, Y. B. He, B. H. Li, F. Y. Kang, *Small* **2017**, *13*, 1602539.

[24] R. Carter, L. Oakes, N. Muralidharan, A. P. Cohn, A. Douglas, C. L. Pint, *ACS Appl. Mater. Interfaces* **2017**, *9*, 7185.

[25] Z. Yuan, H. J. Peng, T. Z. Hou, J. Q. Huang, C. M. Chen, D. W. Wang, X. B. Cheng, F. Wei, Q. Zhang, *Nano Lett.* **2016**, *16*, 519.

[26] J. Pu, Z. H. Shen, J. X. Zheng, W. L. Wu, C. Zhu, Q. W. Zhou, H. G. Zhang, F. Pan, *Nano Energy* **2017**, *37*, 7.

[27] H. H. Xu, A. Manthiram, *Nano Energy* **2017**, *33*, 124.

[28] Q. Pang, D. P. Kundu, L. F. Nazar, *Mater. Horiz.* **2016**, *3*, 130.

[29] T. Y. Lei, W. Chen, J. W. Huang, C. Y. Yan, H. X. Sun, C. Wang, W. L. Zhang, Y. R. Li, J. Xiong, *Adv. Energy Mater.* **2017**, *7*, 1601843.

[30] Z. Y. Wang, Y. F. Dong, H. J. Li, Z. B. Zhao, H. B. Wu, C. Hao, S. H. Liu, J. S. Qiu, X. W. Lou, *Nat. Commun.* **2014**, *5*, 5002.

[31] C. Y. Chen, H. J. Peng, T. Z. Hou, P. Y. Zhai, B. Q. Li, C. Tang, W. C. Zhu, J. Q. Huang, Q. Zhang, *Adv. Mater.* **2017**, *29*, 1606802.

[32] G. Y. Zheng, Q. F. Zhang, J. J. Cha, Y. Yang, W. Y. Li, Z. W. Seh, Y. Cui, *Nano Lett.* **2013**, *13*, 1265.

[33] F. D. Lowy, *N. Engl. J. Med.* **1998**, *8*, 520.

[34] Q. Pang, L. F. Nazar, *ACS Nano* **2016**, *10*, 4111.

[35] J. X. Song, T. Xu, M. L. Gordin, P. Y. Zhu, D. P. Lv, Y. B. Jiang, Y. S. Chen, Y. H. Duan, D. H. Wang, *Adv. Funct. Mater.* **2014**, *24*, 1243.

[36] Y. C. Qiu, W. F. Li, W. Zhao, G. Z. Li, Y. Hou, M. N. Liu, L. S. Zhou, F. M. Ye, H. F. Li, Z. H. Wei, S. H. Yang, W. H. Duan, Y. F. Ye, J. H. Guo, Y. G. Zhang, *Nano Lett.* **2014**, *14*, 4821.

[37] X. L. Ji, K. T. Lee, L. F. Nazar, *Nat. Mater.* **2009**, *8*, 500.

[38] J. J. Varrone, D. Li, J. L. Daiss, E. M. Schwarz, *Int. Bone Miner. Soc. BoneKEy* **2011**, *4*, 187.

[39] Y. C. Zhang, Y. You, S. Xin, Y. X. Yin, J. Zhang, P. Wang, X. S. Zheng, F. F. Cao, Y. G. Guo, *Nano Energy* **2016**, *25*, 120.

[40] X. X. Peng, Y. Q. Lu, L. L. Zhou, T. Sheng, S. Y. Shen, H. G. Liao, L. Huang, J. T. Li, S. G. Sun, *Nano Energy* **2017**, *32*, 503.

[41] H. R. Pant, S. P. Adhikari, B. Pant, M. K. Joshi, H. J. Kim, C. H. Park, C. S. Kim. *J. Colloid Interface Sci.* **2015**, *457*, 174.

[42] M. P. Yu, R. Li, Y. Tong, Y. R. Li, C. Li, J. D. Hong, G. Q. Shi, *J. Mater. Chem. A* **2015**, *3*, 9609.

[43] M. P. Yu, J. S. Ma, H. Q. Song, A. J. Wang, F. Y. Tian, Y. S. Wang, H. Qiu, R. M. Wang, *Energy Environ. Sci.* **2016**, *9*, 1495.

[44] J. R. Pels, F. Kapteijn, J. A. Moulijn, Q. Zhu, K. M. Thomas, *Carbon* **1995**, *33*, 1641.

[45] L. F. Lai, J. R. Potts, D. Zhan, L. Wang, C. K. Poh, C. H. Tang, H. Gong, Z. X. Shen, J. Y. Lin, R. S. Ruoff, *Energy Environ. Sci.* **2012**, *5*, 7936.

[46] M. F. Chen, S. X. Jiang, C. Huang, X. Y. Wang, S. Y. Cai, K. X. Xiang, Y. P. Zhang, J. X. Xue, *ChemSusChem* **2017**, *10*, 1.

[47] Q. Pang, J. T. Tang, H. Huang, X. Liang, C. Hart, K. C. Tam, L. F. Nazar, *Adv. Mater.* **2015**, *27*, 6021.

[48] K. Mi, S. W. Chen, B. J. Xi, S. S. Kai, Y. Jiang, J. K. Feng, Y. T. Qian, S. L. Xiong, *Adv. Funct. Mater.* **2017**, *27*, 1604265.

[49] Y. Zhang, C. W. Wang, H. S. Hou, G. Q. Zou, X. B. Ji, *Adv. Energy Mater.* **2017**, *7*, 1600173.

[50] Q. Pang, D. P. Kundu, M. Cuisinier, L. F. Nazar, *Nat. Commun.* **2014**, *5*, 4759.

[51] J. Q. Huang, Z. Y. Wang, Z. L. Xu, W. G. Chong, X. Y. Qin, X. Y. Wang, J. K. Kim, *ACS Appl. Mater. Interfaces* **2016**, *8*, 28663.

[52] Z. Liang, G. Y. Zheng, W. Y. Li, Z. W. Seh, H. B. Yao, K. Yan, D. S. Kong, Y. Cui, *ACS Nano* **2014**, *8*, 5249.

[53] Y. Yang, G. Y. Zheng, Y. Cui, *Chem. Soc. Rev.* **2013**, *42*, 3018.

[54] F. Pei, T. H. An, J. Zang, X. J. Zhao, X. L. Fang, M. S. Zheng, Q. F. Dong, N. F. Zheng, *Adv. Energy Mater.* **2016**, *6*, 1502539.

[55] Z. B. Xiao, Z. Yang, L. Wang, H. G. Nie, M. Zhong, Q. Q. Lai, X. J. Xu, L. J. Zhang, S. M. Huang, *Adv. Mater.* **2015**, *27*, 2891.

[56] Y. Y. Li, Q. F. Cai, L. Wang, Q. W. Li, X. Peng, B. Gao, K. F. Huo, P. K. Chu, *ACS Appl. Mater. Interfaces* **2016**, *8*, 23784.

[57] G. M. Zhou, Y. B. Zhao, C. X. Zu, A. Manthiram, *Nano Energy* **2015**, *12*, 240.

[58] D. V. Bavykin, J. M. Friedrich, F. C. Walsh, *Adv. Mater.* **2006**, *18*, 2807.

[59] M. L. Sushko, K. M. Rosso, J. Liu, *J. Phys. Chem. C* **2010**, *114*, 20277.

[60] X. Liang, C. Y. Kwok, F. L. Marzano, Q. Pang, M. Cuisinier, H. Huang, C. J. Hart, D. Houtarde, K. Kaup, H. Sommer, T. Brezesinski, J. Janek, L. F. Nazar, *Adv. Energy Mater.* **2016**, *6*, 1501636.

[61] G. M. Zhou, H. Z. Tian, Y. Jin, X. J. Tao, B. F. Liu, R. F. Zhang, Z. W. Seh, D. Zhou, Y. Y. Liu, J. Sun, J. Zhao, C. X. Zu, D. S. Wu, Q. F. Zhang, Y. Cui, *Proc. Natl. Acad. Sci.* **2017**, *114*, 840.